

Spectrum Tailored Defective 2D Semiconductor Nanosheets Aerogel for Full-Spectrum-Driven Photothermal Water Evaporation and Photochemical Degradation

Min-Quan Yang, Chuan Fu Tan, Wanheng Lu, Kaiyang Zeng, and Ghim Wei Ho*

The wide spectral range of the solar flux with undesirable diffused energy distribution remains a substantial impediment to the high-efficiency utilization of the whole spectrum. Here, inspired by the spectrally selective sunlight utilization of plants, a spectrum-tailored solar harnessing aerogel is conceived. It is composed of oxygen vacancy (O_v) defect-rich semiconductor HNb_3O_8 (D- HNb_3O_8) nanosheets and polyacrylamide (PAM) framework to perform all-in-one photochemical and photothermal full solar energy conversion. The aerogel selectively utilizes the whole solar spectrum, in which high energy ultraviolet (UV) photon is converted into high redox potential electron–hole pairs, while low energy visible-near infrared (NIR) photons are transformed into heat. The designed solar absorber-polymer composite shows energy harnessing-conversion capability with desired heat insulation, reactant enrichment, rapid mass diffusion and capillary pumping characteristics, thus realizing a high efficient steam generation and photochemical activity. This cooperative photochemical and photothermal solar energy conversion, at respective optimal working spectrum, holds great promise for optimizing and maximizing the solar energy utilization, as well as opening up opportunities to explore simultaneous multifunctional usage of solar energy.

1. Introduction

Exploring high-efficiency solar energy conversion techniques and materials has been an enduring theme of human society.^[1] Typically, photochemical and photothermal transformations are two fundamental schemes underlying the harnessing and utilization of solar energy.^[1a] Photochemical conversion generally involves the capturing of sunlight by solar absorbers to excite

charge carriers, which then migrate and react with target molecules. The scheme is attractive for its versatility in direct chemicals, fuels production and polluted environments restoration.^[2] However, its commercial viability is hampered by some principle challenges including limited ultraviolet (UV)-visible solar light absorption (generally < 600 nm) and sluggish charge transfer dynamics.^[3] Alternatively, photothermal transformation is a distinct strategy that harnesses solar photon to generate heat, which can be used to power catalytic reactions^[4] and other functions such as domestic heating and water distillation/desalination^[5] that is attractive to fresh water production,^[6] thereby realizing the transformation and storage of solar energy. Compared to the photochemical conversion, the photothermal approach displays prominent advantage in visible-near infrared (NIR) light harvesting. It is favorable to capture a broad solar spectrum. Nevertheless, the nonselective full

conversion of the solar energy to heat poses an inevitable loss of downgrading the energy quality of the high-frequency solar photons, particularly for the UV light band. Moreover, the UV light-induced heating effect is much weaker than that of visible–NIR light due to its low proportion ($\approx 5\%$) in the whole solar spectrum. This further devalues the conversion of high frequency solar photon to heat. In this context, to promote and optimize the utilization of the entire solar energy, development of efficient strategy and material system that could pertinently address different wavelength of the solar photons, i.e., UV and visible–NIR photons, is highly sought after.

Here, we explore a spectrally selective utilization strategy to promote the solar energy conversion by designating photochemical and photothermal conversion to their optimal working spectra in a unified material system. Such approach is inspired by plants, for which high-frequency solar photon is captured to power photosynthetic process for chemicals and fuels production, while low-frequency solar photon is transformed into heat to drive transpiration, thereby optimally utilizing the broad solar spectrum with high conversion efficiency. To mimic the spectrum-tailored all-in-one solar conversion scheme of plants, a defective semiconductor nanosheets aerogel comprises of oxygen vacancy (O_v) defect-rich HNb_3O_8 nanosheets (D- HNb_3O_8) and a polymeric polyacrylamide (PAM) network is constructed, as illustrated

Dr. M.-Q. Yang, C. F. Tan, Dr. W. Lu, Prof. G. W. Ho
Department of Electrical and Computer Engineering
National University of Singapore
4 Engineering Drive 3, Singapore 117583, Singapore
E-mail: elehgw@nus.edu.sg

Prof. K. Zeng
Department of Mechanical Engineering
National University of Singapore
9 Engineering Drive 1, Singapore 117576, Singapore

Prof. G. W. Ho
Department of Materials Science and Engineering
National University of Singapore
9 Engineering Drive 1, Singapore 117575, Singapore

 The ORCID identification number(s) for the author(s) of this article can be found under <https://doi.org/10.1002/adfm.202004460>.

DOI: 10.1002/adfm.202004460

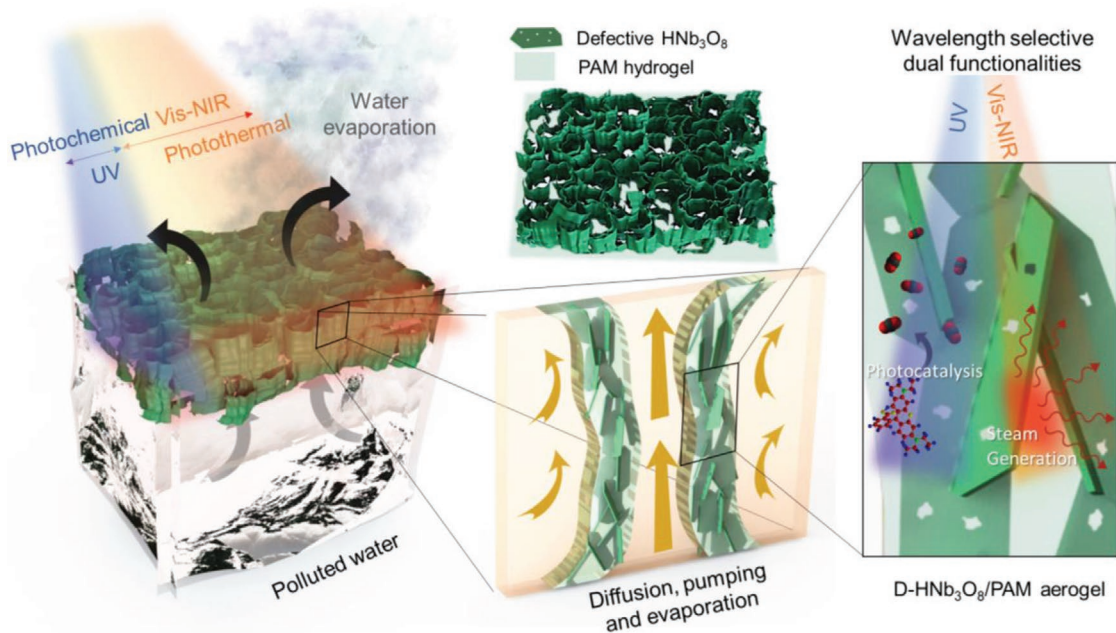


Figure 1. Schematic illustration of the synchronous photothermal and photochemical solar conversion of a defective D-HNb₃O₈/PAM aerogel.

in **Figure 1**. The Nb-based nanosheets possess advantages of high photoactivity and easily functionalized 2D structure with large exposure of surface active sites.^[7] On the other hand, the PAM has the ease of processing in regards to polymerization and cross-linking.^[8] Also, it is relatively low-cost and solution based mass-producible, critical towards practical application.^[9]

Through the ingenious integration of D-HNb₃O₈ with PAM, the constructed hybrid aerogel inherits both the desirable properties and structural merits of the respective building blocks. Specifically, the D-HNb₃O₈ absorbs the full solar spectrum to perform two disparate spectrally selective functions of UV-driven photocatalytic excitation and visible–NIR induced photothermal heating. The hydrophilic PAM chains form an interconnected thermal insulation porous structure with capillary pumping capability to minimize heat loss and supply adequate water for continuous solar vapor generation. In addition, the microporous PAM frameworks display strong adsorption capability for wicking and capturing reactant molecules. More importantly, benefiting from the homogeneously infiltrated D-HNb₃O₈ solar absorber in the PAM polymeric matrix, the harvested and converted solar energy over D-HNb₃O₈ can be directly delivered to the captured molecules absorbed on the PAM chains and water confined in the molecular meshes. Besides, the localized solar heat induced by thermal insulation of PAM could accelerate the photochemical reaction due to the near-field temperature increase surrounding the D-HNb₃O₈-reactant complexes, thus synergistically facilitating all-in-one photochemical and photothermal conversion. Ultimately, the dual-spectrum responsive aerogel synchronously demonstrates a high solar steam generation rate of 1.4 kg m⁻² h⁻¹ with a solar thermal conversion efficiency up to 91%, in parallel to photocatalytic degradation under 1 sun irradiation (1 kW m⁻²). This result suggests a promising avenue to maximize solar energy utilization for multifunctional applications.

2. Results and Discussion

The defective D-HNb₃O₈ semiconductor nanosheets with abundant O_v used for the aerogel construction are prepared via a facile light-induced hydrogenation method in the presence of Pd (Methods, Supporting Information).^[10] **Figure 2a,b** shows the atomic force microscopy (AFM) image and height profiles of the D-HNb₃O₈, which reveals a uniform nanosheet morphology with a thickness of about 1.2 nm, corresponding to a thin monolayer HNb₃O₈ structure.^[7b] Transmission electron microscopy (TEM) analysis discloses that metallic Pd nanoparticles with distinct lattice fringes of 0.23 nm are well-dispersed on the ultrathin D-HNb₃O₈ nanosheets (Figure 2c,d).^[11] Importantly, the high resolution TEM (HRTEM) image shows localized lattice disorder on the monolayer D-HNb₃O₈ nanosheets (Figure 2e; Figure S1, Supporting Information). This can be ascribed to the generation of abundant O_v defects during the hydrogenation treatment, which causes charge reconstruction and alters the electronic and geometric structures of the nanosheets. As confirmed in Figure 2f, the low temperature electron paramagnetic resonance (EPR) analysis of the D-HNb₃O₈ samples display a strong peak at $g = 2.003$ assigned to O_v,^[12] directly validating the generation of O_v. Moreover, the O_v signal is observed to increase with Pd content, indicating a controllable manipulation of the O_v content. The characterizations collectively demonstrate the reduction of the monolayer HNb₃O₈ with the creation of abundant O_v.

In the following, PAM is adopted as a matrix to interconnect the defective D-HNb₃O₈ nanosheets due to its easy gelation, high transparency and hydrophilicity.^[8,13] **Figure 3a** schematically illustrates the synthesis process (Methods, Supporting Information). Scanning electron microscopy (SEM) images of the defective D-HNb₃O₈/PAM aerogel from top view and

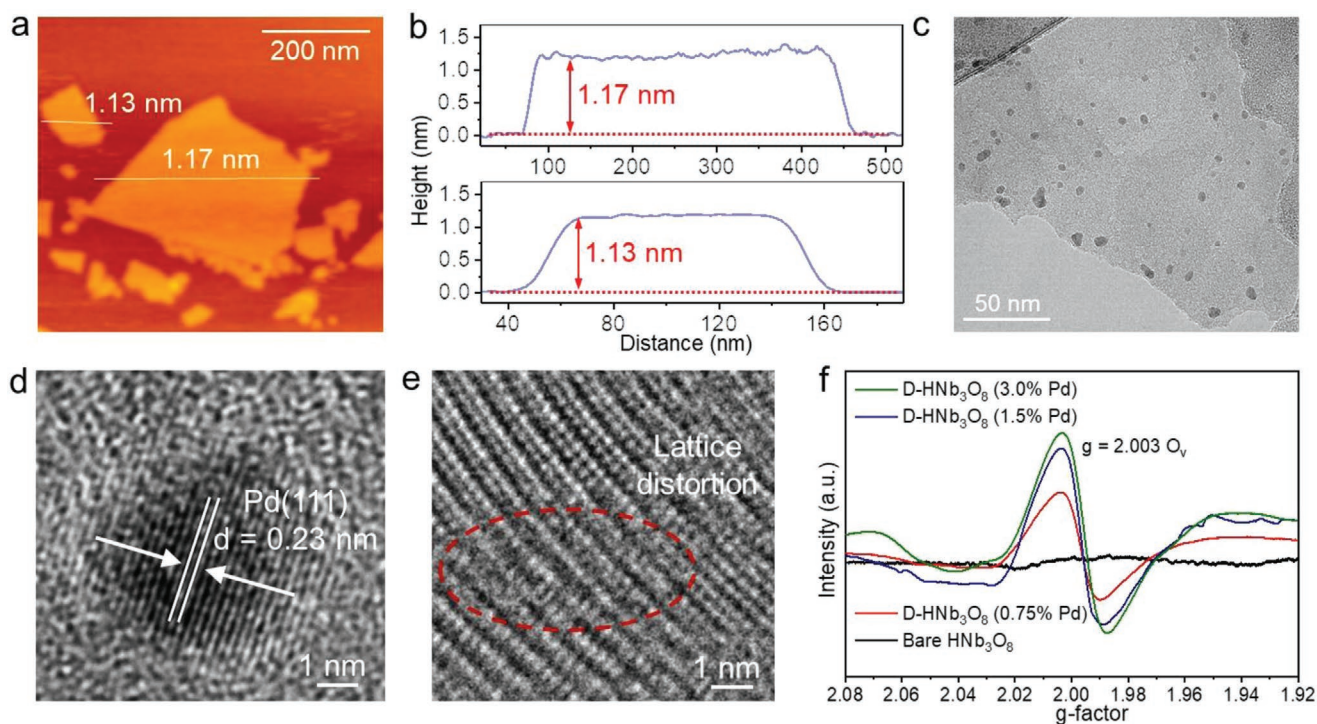


Figure 2. a) AFM image and b) corresponding height profiles of D-HNb₃O₈; c) TEM image and d,e) HRTEM images of D-HNb₃O₈; f) low temperature EPR spectra of bare HNb₃O₈ and D-HNb₃O₈ samples.

side view (Figure 3b,c) both present a highly interconnected microporous structure with several micrometers pore sizes. Analogous microporous structure is observed in pure PAM aerogel (Figure S2, Supporting Information). This indicates that the defective D-HNb₃O₈ nanosheets have no significant influence on the gelation of PAM, which crosslinks and immobilizes the nanosheets to form a supportive 3D framework. Figure 3d displays the wall structure of the aerogel. It clearly indicates the presence of wrinkles on the surface attributed to the shrinkage of the polymeric PAM skeleton caused by the dehydration of the hydrogel.^[14]

Moreover, Figure 3e,f show TEM images of the D-HNb₃O₈/PAM. Pd nanoparticles with diameters of 2–5 nm are well dispersed on the nanosheets (marked with red circles). Energy-dispersive X-ray spectroscopy (EDX) mappings reveal that C, N, Nb, O and Pd elements are uniformly distributed throughout the aerogel sheet structure (Figure 3g), denoting that the D-HNb₃O₈ nanosheets are successfully incorporated into the polymeric PAM. The weak signal of Pd should be ascribed to its low content. Additionally, Fourier transform infrared spectrum (FTIR) analysis of the D-HNb₃O₈/PAM reveals both characteristic absorption peaks of D-HNb₃O₈^[15] and PAM^[16] (Figure 4a), also indicating the successful coupling of D-HNb₃O₈ nanosheets and PAM polymer. Furthermore, the porosity of the aerogels has been measured by liquid displacement method,^[17] which all display large values of around 90% (Figure S3, Supporting Information). The high porosity endows the aerogels with low apparent density ($\approx 5.0 \text{ mg cm}^{-3}$) (Equation S1, Supporting Information), enabling them to stay afloat in the water, beneficial for interfacial water heating. All the above complementary findings conclude

that a 3D interconnected porous aerogel structure with cross-linked defective semiconductor nanosheets and PAM polymer has been established, which features micrometers channels, in-built wrinkled surface, and molecular meshes (polymer network).

Broadband light capture with high absorption capability is a critical factor for solar energy conversion. To evaluate the optical absorption property, UV–vis–NIR diffuse reflectance spectroscopy (DRS) is employed. As shown in Figure 4b and Figure S4 (Supporting Information), the hybrid D-HNb₃O₈/PAM aerogels with abundant defects exhibit excellent light absorption throughout the solar spectrum (250–2500 nm). The D-HNb₃O₈/PAM (1.5% Pd) shows $\approx 90\%$ absorption of the solar energy (optical transmittance $< 0.1\%$ and reflectance $\approx 10\%$, Figure S5, Supporting Information), which is significantly higher than that of HNb₃O₈/PAM without defects. The enhanced light absorption is also visually observable (Figure S6, Supporting Information). Notably, the bare PAM is transparent, verifying that defective D-HNb₃O₈ is the main photoactive component. The result reveals the significant role of the defect in promoting the solar energy capture. Further increase of Pd content from 1.5% to 3.0% results in less light absorption enhancement due to the saturation of defect content (Figure S4, Supporting Information). Additionally, a control sample of D-HNb₃O₈/PAM (1.5% Pd) film is fabricated for comparison. It shows a much lower light absorption of $\approx 70\%$ in the whole solar region than the D-HNb₃O₈/PAM aerogels owing to the tightly packed 2D layer-by-layer assembled structure (Figures S7 and S8, Supporting Information). The finding highlights the advantage of the 3D microporous structure in promoting the solar energy harvesting.

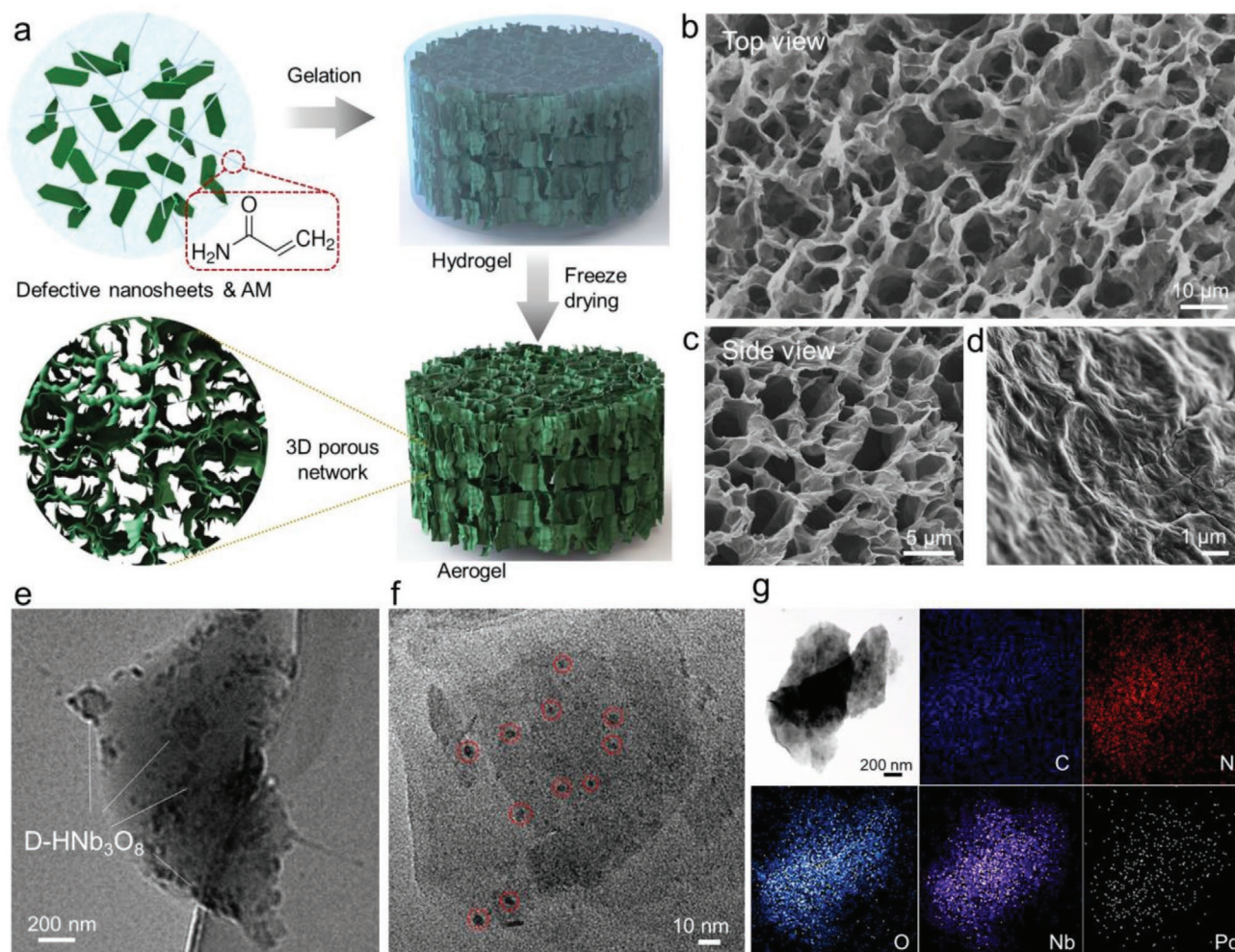


Figure 3. a) Schematic illustration for the synthesis of the defective D-HNb₃O₈/PAM aerogel; b–d) SEM images of the aerogel; e, f) TEM images and g) EDX mapping analysis of the aerogel.

Moreover, to assess the water transportation performance, water contact angle, saturated water content (Q_s) and half swollen time (T) have been measured. As shown in Figure S9 (Supporting Information), the contact angle measurement shows that the D-HNb₃O₈/PAM aerogel can be wetted within ≈ 3 s, demonstrating super hydrophilicity. Analogous results are observed for bare PAM and D-HNb₃O₈ film. The excellent wettability is conducive to water flow and vapor escaping.^[5h,9] Figure 4c shows the Q_s of the aerogels, which display similar values of ≈ 11 g g⁻¹ due to their analogous structure (Equation S2, Supporting Information), implying a high swelling capacity. By recording the swollen time from half-saturated state ($0.5Q_s$) to saturated state, the T values of the aerogels are determined to be around 5 min (Figure S10, Supporting Information).^[14,18] Based on the Q_s and T , the water transport rate is evaluated to be around 2.3 g min⁻¹ (Equation S3, Supporting Information),^[14,18] representing excellent water transport property. However, it is notable that for the D-HNb₃O₈/PAM film counterpart, the water transport rate is ≈ 0.02 g min⁻¹, which is markedly smaller than the aerogel structure. Due to that the aerogel and film samples display similar wettability,

which are all super hydrophilicity, the significantly higher water transport ability of the aerogels can be ascribed to their porous structure, high surface roughness, and molecular mesh. These features effectively increase the contact area with the water molecules, enabling efficient mass transportation.

Besides light absorption and water transportation, thermal transport performance is also critical for solar-to-thermal conversion. Figure 4d shows the thermal conductivities of the samples. All the defective aerogels display low thermal conductivity of about 0.04 W m⁻¹ K⁻¹, which is lower than that of pure water (0.06 W m⁻¹ K⁻¹ at 300 K).^[19] The value is also comparable to most of the recently reported advanced insulating materials utilized in solar thermal evaporation such as cellulose membrane,^[20] wood,^[21] carbon-based aerogels^[17a] and airlaid paper (0.02–0.05 W m⁻¹ K⁻¹).^[22] The thermal insulation performance of the aerogel is also evaluated by a heating experiment (Figure 4e). When the aerogel is placed on a hot plate at 200 °C for an extended time of 10 min to reach a stable state, the temperature of the top side of the aerogel is 140 °C lower than that of the bottom side. Additionally, compared to the aerogel, the D-HNb₃O₈ film displays a significantly higher thermal

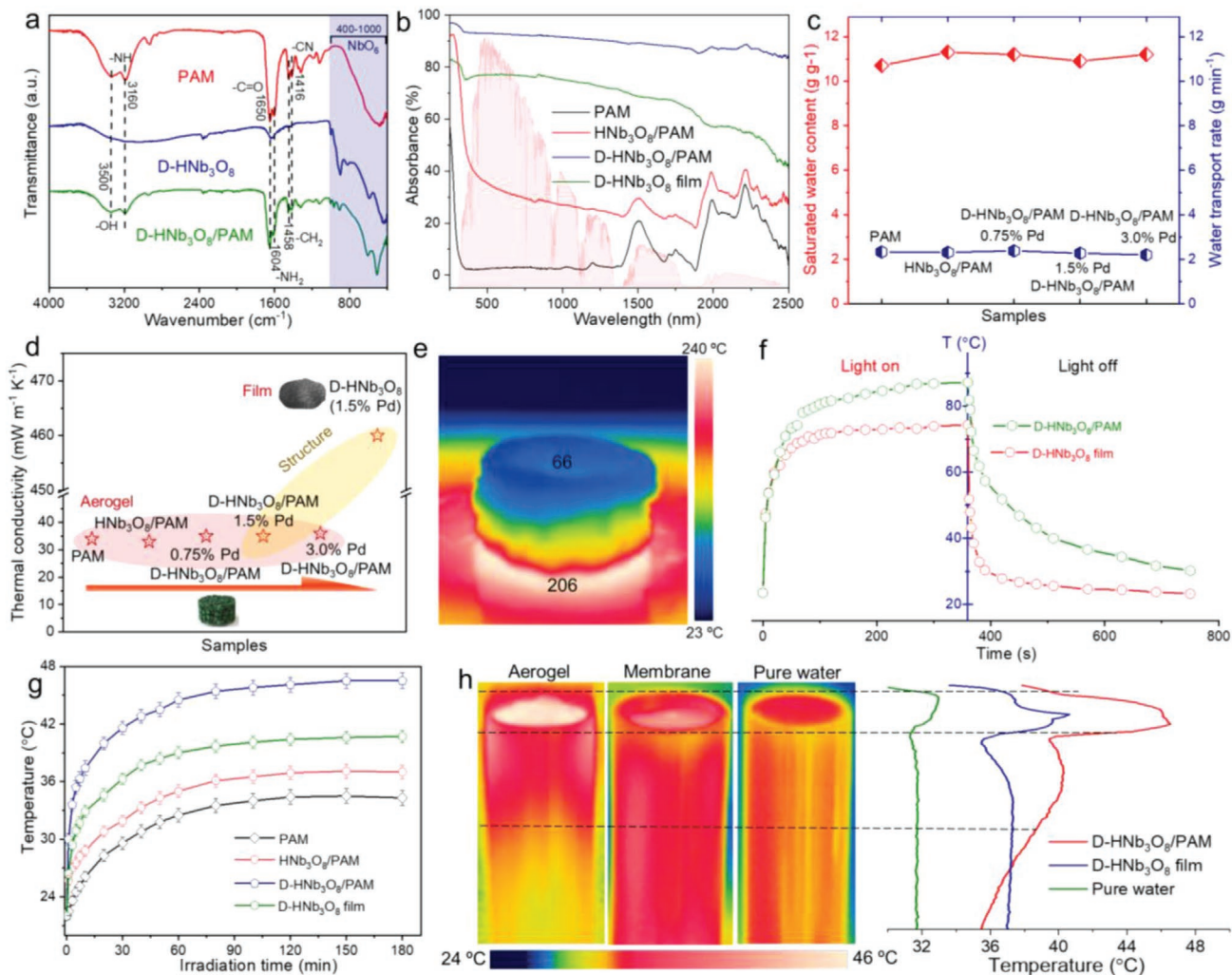


Figure 4. a) FTIR spectra of the PAM, D-HNb₃O₈ and hybrid D-HNb₃O₈/PAM; b) light absorption of the as-synthesized samples; c) saturated water content and calculated water transport rate of the aerogel samples; d) thermal conductivities of the bare PAM, D-HNb₃O₈/PAM aerogel composites and D-HNb₃O₈ film; e) thermographic image of an aerogel positioned on a hot plate with a surface temperature of about 200 °C; f) temperature changes of D-HNb₃O₈/PAM aerogel and film under 1 kW m⁻² light irradiation; g) surface temperature changes of different samples in water; and h) temperature profiles of water-air interface with aerogel, film and without sample.

conductivity of 0.45 W m⁻¹ K⁻¹. This is due to the absence of the PAM and microporous structure in the film, which results in a fast heat transfer from the film to the surrounding environment.

The defining advantage of 3D microporous structure has endowed the defective aerogel with remarkable photothermal conversion performance than the 2D film under both dry and wet conditions. As shown in Figure 4f, the dry aerogel can be heated up to 87 °C within 6 min under 1 sun irradiation and finally reaches a steady state temperature of 92 °C after 30 min (Figure S11, Supporting Information). It is about 13 and 16 °C higher than that of the film, respectively. More importantly, the aerogel displays a significantly slower cooling rate than the film when the simulated solar light is switched off. Similar result is observed after soaking the aerogel and film in water (Figure 4g). The stable surface temperature of the aerogel is about 6 °C higher than that of the film. Temperature-depth analysis of the samples in water reveals that the defective aerogel exhibits

a sharply localized heat confinement at the evaporative surface. On the contrary, the pure water and the film system both show much smaller differences between the surface and the bulk water (Figure 4h). The results demonstrate greatly enhanced photothermal conversion by virtue of heat insulation and localization of the 3D porous aerogel structure, which is favorable for minimizing heat loss and augmenting solar-thermal conversion efficiency.

Noticeably, without visible–NIR light, the UV light irradiation alone induces a smaller temperature increase (Figure S12, Supporting Information), implying that the significant solar heating effect is generated from the visible–NIR photon conversion. This can be explained by a few reasons. Firstly, the UV photon only accounts for a low portion of about 5% in the whole solar spectrum.^[3,23] Secondly, the UV photon captured by the D-HNb₃O₈ nanosheets is liable to be converted to high redox potential charge carriers rather than heat. This has

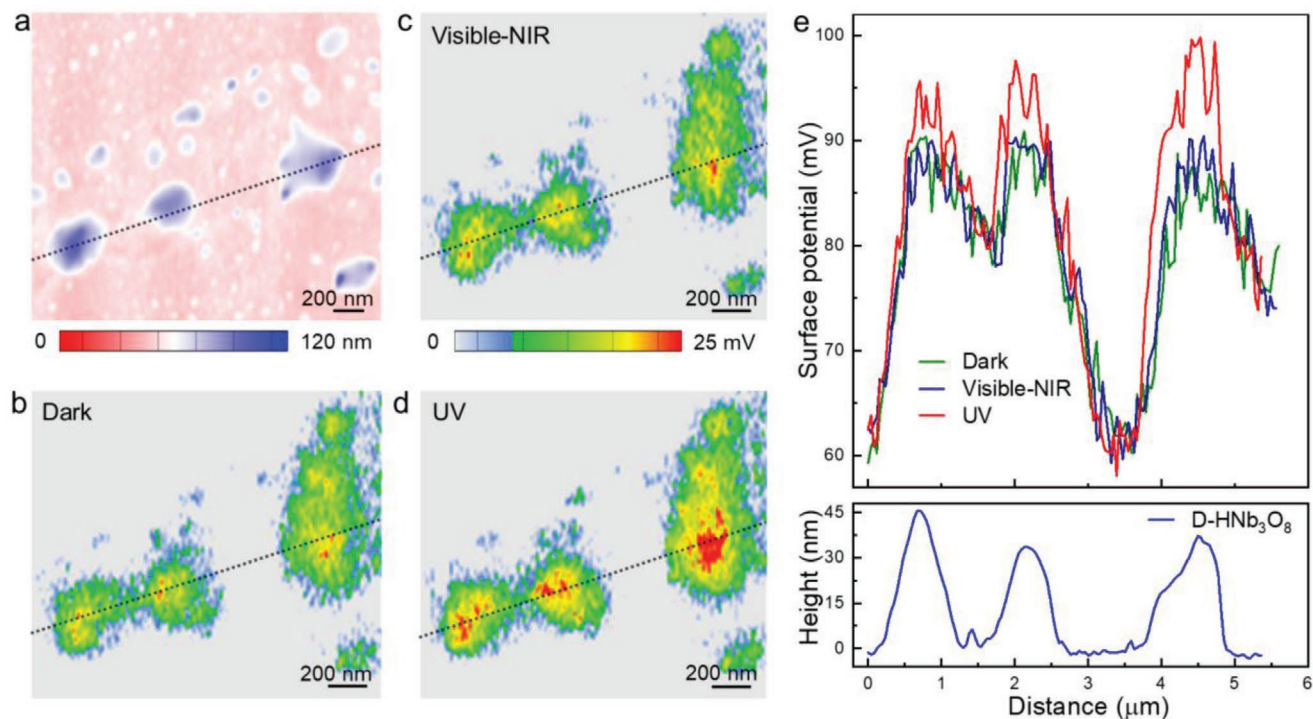


Figure 5. a) Topographic image and b-d) surface potential mappings in the dark, or under visible–NIR and UV light illumination of D-HNb₃O₈ nanosheets; e) the cross-section profiles and corresponding height profile of D-HNb₃O₈ nanosheets.

been verified by photoelectrochemical test. As displayed in Figure S13 (Supporting Information), under full solar light irradiation, a noticeable photocurrent response is observed for the D-HNb₃O₈, indicating an efficient electron–hole pairs generation and separation. Wavelength-dependent experiments unveil that the photocurrent generation is dominated by UV light rather than the visible–NIR light.

Moreover, light-irradiated Kelvin Probe Force Microscope (KPFM) analysis of D-HNb₃O₈ nanosheets has been further performed. It can directly detect the photo-induced surface potential (SP) variations over sample surface, thus disclosing the changes of the surface charge density due to the generation, separation, and transfer of charges under light.^[24] Figure 5a–d shows the topographic image and KPFM images of the D-HNb₃O₈ distributed on a Pt-coated silicon wafer in the dark or illuminated by visible–NIR and UV light. Under visible–NIR light irradiation, the SP of the D-HNb₃O₈ nanosheets is almost same to that under dark condition, implying that no effective charge carriers are generated. In contrast, a distinct SP increase is observed on D-HNb₃O₈ nanosheets when the sample is illuminated by UV light (Figure 5e). The improved SP is due to the photoexcitation, in which the generated electrons are captured by Pt-coated silicon wafer, while the holes are accumulated on the surface of D-HNb₃O₈. The KPM results, in combination with the photothermal conversion test, clearly demonstrate the spectrally selective solar light utilization of the D-HNb₃O₈/PAM aerogel. This is mainly caused by the production of localized O_v in the ultrathin D-HNb₃O₈ nanosheets, which forms crystalline order domains and highly disorder “nanoislands.”^[10b] The ordered structure retains the benefits of crystalline HNb₃O₈ to absorb high energy UV photon for charge carriers excitation,

while the disordered region yield new gap states that captures low energy visible–NIR photon for heat production, as illustrated in Figure 6a.

Consequently, as demonstrations, the aerogels have been systematically investigated for two solar-driven model reactions of interfacial solar-driven steam generation and photocatalytic degradation. Figure 6b displays the photocatalytic performance of the samples. The bare PAM aerogel shows negligible activity under 1 sun irradiation due to its incapability in generating redox charge carriers. With the introduction of HNb₃O₈/PAM, about 60% rhodamine B (RhB) is degraded after 120 min. Further photoactivity enhancement is observed for the D-HNb₃O₈/PAM with 1.5% Pd, which fully oxidizes the RhB within 100 min. The activity outperforms typical TiO₂ and ZnO photocatalysts (Figure S14, Supporting Information), indicating a high photochemical activity of the aerogel. Higher Pd content of the defective aerogel results in reduced photodegradation activity (Figure S15, Supporting Information) pertaining to increased recombination of charge carriers.^[10b] Notably, D-HNb₃O₈/PAM film merely shows 15% degradation of RhB within 120 min. This can be attributed to the greatly reduced surface area and aggregated structure in the film, which lowers the adsorption and inhibits the transportation of reactant molecules. As shown in Figure S16 (Supporting Information), the adsorption experiment shows that the aerogel can enrich 32% more of the reactant in its microporous structure than the film. Given the crucial role of the reactant adsorption in heterogeneous catalysis,^[25] the stratagem of capturing the reactant molecules in the aerogel would greatly promote the surface redox reaction rate, thereby enhancing the photochemical conversion performance. The result highlights the contribution of the porous aerogel structure for promoting photochemical conversion.

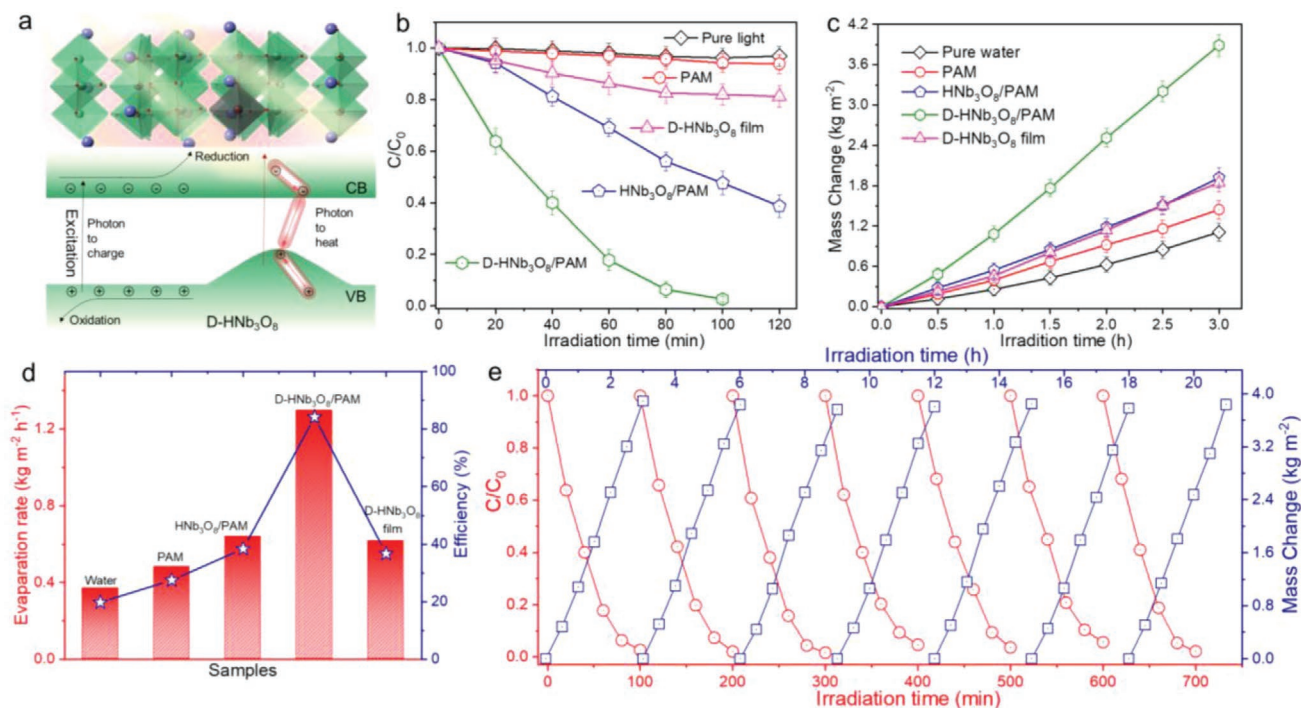


Figure 6. a) Schematic illustration of spectrally selective utilization of full solar energy over the D-HNb₃O₈; b) photocatalytic performance of the series of samples for photochemical RhB degradation; c) photothermal steam generation of different samples under 1 kW m⁻²; d) the evaporation rates and corresponding solar to thermal conversion efficiencies of the samples; e) recyclability of the D-HNb₃O₈/PAM aerogel for photochemical degradation and photothermal steam generation.

Moreover, spectrum-controlled experiment shows that under UV light irradiation, the aerogel can degrade about 70% RhB within 100 min, whereas the visible–NIR light irradiation results in negligible catalytic degradation ($\approx 3\%$) (Figure S17, Supporting Information). The obvious UV light photoactivity is initiated by the photoinduced charge carriers with high redox capability. On the contrary, considering that the visible–NIR photon energy is insufficient to generate high redox potential charge carriers, the inferior visible–NIR photoactivity should originate from the photosensitization of RhB molecule. This is in good accordance with the photoelectrochemical analysis. Besides, it is noteworthy that the full spectrum photoactivity of the aerogel is higher than the sum up photochemical activities induced by individual UV and visible–NIR light. This should be attributed to a synergistic effect between the UV excitation and visible–NIR heating in performing the photochemical conversion.^[10b,26] Previous studies have shown that the introduction of heat to photocatalytic process would greatly promote the photochemical conversion by providing high kinetic energy to the photogenerated electron–hole pairs and the reactants.^[10b,26,27] This in turn improves the charge carriers mobility, inhibits their recombination and increases the number of energetic interactions. The D-HNb₃O₈/PAM aerogel with incorporated defects is designed to simultaneously convert solar photons into charge carriers and heat. Particularly, the generated heat is favorably confined due to the low thermal conductivity of the aerogel. This would greatly enhance the localized near-field photoheating of the D-HNb₃O₈-reactant complexes to immensely promote photochemical conversion.

Furthermore, the photothermal conversion performance of the aerogel has been evaluated by solar steam generation. Water can be rapidly transported from the bulk water to the aerogel by capillary action through its open cell structure. The solar steam generation performance is quantified by recording the mass loss of water over time (Figure 6c). In the absence of any solar absorber, the pure water shows an evaporation rate of 0.370 kg m⁻² h⁻¹, in line with the reported results.^[5a,28] The noticeable evaporation rate can be attributed to the absorption of NIR light above 900 nm by the water.^[28] Bare PAM aerogel shows slight enhancement in the water evaporation rate (0.482 kg m⁻² h⁻¹) as compared to the pure water system, which can be ascribed to its transparent nature with limited light absorption. By contrast, the water evaporation rate substantially improves for the aerogels from 0.640 kg m⁻² h⁻¹ of HNb₃O₈/PAM to 0.951, 1.297, and 1.401 kg m⁻² h⁻¹ of the D-HNb₃O₈/PAM solar absorbers with gradually increased defect content (Figure 6c; Figure S18, Supporting Information). This aligns well with the light absorption enhancement and temperature change of the D-HNb₃O₈/PAM aerogels (Figures S4 and S19, Supporting Information).

Based on the evaporation rate, the corresponding solar energy conversion efficiency (η) for the steam generation has been calculated (Equations S4 and S5, Supporting Information). The defective aerogels show much higher η values than the counterpart samples, as displayed in Figure 6d and Figure S20 (Supporting Information). The solar to vapor generation efficiency for the 1.5% Pd aerogel is determined to be 84.1%, which can increase to 91% with 3.0% Pd. The

performance is comparable to recently reported state-of-the-art material systems (Table S1, Supporting Information).^[5h,i,29] The heat loss of the aerogel, including conduction, radiation, and convection,^[5h,19a,30] is calculated to be $\approx 7.05\%$ under 1 kW m^{-2} solar irradiation (Equations S6-S8, Supporting Information). In addition, the η value of the optimal D-HNb₃O₈/PAM aerogel is about 71% and 64% higher than that of the pure water and bare PAM aerogel, respectively. Likewise, the performance of the aerogel is also much better than the film sample ($0.616 \text{ kg m}^{-2} \text{ h}^{-1}$) with a solar conversion efficiency of 36.7% under the same condition. The result further highlights the structural advantage of the aerogel in promoting solar energy utilization, not only for photochemical utilization, but also for the photothermal conversion.

Finally, continuous photochemical and photothermal conversion measurement has been carried out to assess the recyclability of the aerogel. Taking the photoactivity and solar thermal conversion performance into account, 1.5% Pd aerogel is adopted for characterizations. After repeating the test for 7 cycles, the aerogel shows no obvious deterioration of the photodegradation and water evaporation abilities (Figure 6e). Moreover, the macro and micro structure analysis of the used aerogel retains its original monolithic and porous structure (Figure S21, Supporting Information), suggesting its high recyclability and mechanical stability. Furthermore, simultaneous photocatalytic degradation of RhB and photothermal steam generation of the D-HNb₃O₈/PAM under salt concentration of $\approx 3.5 \text{ wt}\%$ (with the addition of NaCl) has been carried out to study the effect of salt ions on the performances and structure of the aerogel. As shown in Figure S22 (supporting information), the photochemical and photothermal tests reveal fairly stable degradation activity and evaporation rate of the D-HNb₃O₈/PAM in the presence of salt. In addition, the microstructure analysis of the aerogel after the test shows well retained porous structure. The results indicate that the moderate salt concentration has no critical influence on the aerogel performance.

3. Conclusion

In summary, we have demonstrated an optimal utilization of the whole solar spectrum with high conversion efficiency using a hybrid defective HNb₃O₈ aerogel that consists of ultrathin O_v defect rich semiconductor D-HNb₃O₈ nanosheets cross-linked by PAM. Contrasting from the traditional solitary photochemical and photothermal conversion systems that suffer from the limitations of insufficient solar light capture or trade-offs in the quality of the solar photon, the defective D-HNb₃O₈/PAM aerogel judiciously capitalizes high energy UV photon for redox reactivity, while transforms low energy visible–NIR light into heat. Meanwhile, the PAM forms hydrophilic porous framework with molecular meshes that warrant low thermal conductivity, rapid water transportation and organic molecules enrichment. With the integral design of spectrally selective catalytic and thermal insulative gel, the harnessed solar energy can be directly channeled to the absorbed organic molecules and water for all-in-one solar driven high-performance steam generation and photocatalytic degradation activity. This work

provides a feasible way to maximize the harvesting of sustainable solar energy for multifunctional applications.

Supporting Information

Supporting Information is available from the Wiley Online Library or from the author.

Acknowledgements

This work was supported by Singapore Ministry of Education (MOE) grants (R-263-000-D18-112 and R-263-000-D08-114).

Conflict of Interest

The authors declare no conflict of interest.

Keywords

defective aerogels, full solar spectrum, photochemical degradation, photothermal evaporation, spectrally selective utilization

Received: May 24, 2020

Revised: June 22, 2020

Published online: September 6, 2020

- [1] a) J. Gong, C. Li, M. R. Wasielewski, *Chem. Soc. Rev.* **2019**, *48*, 1862; b) D.-J. Xue, S.-C. Liu, C.-M. Dai, S. Chen, C. He, L. Zhao, J.-S. Hu, L.-J. Wan, *J. Am. Chem. Soc.* **2017**, *139*, 958.
- [2] a) M.-Q. Yang, Y.-J. Xu, W. Lu, K. Zeng, H. Zhu, Q.-H. Xu, G. W. Ho, *Nat. Commun.* **2017**, *8*, 14224; b) A. Li, T. Wang, C. Li, Z. Huang, Z. Luo, J. Gong, *Angew. Chem., Int. Ed.* **2019**, *58*, 3804; c) J. Ran, G. Gao, F.-T. Li, T.-Y. Ma, A. Du, S.-Z. Qiao, *Nat. Commun.* **2017**, *8*, 13907; d) Y. Zhao, Y. Zhao, R. Shi, B. Wang, G. I. N. Waterhouse, L.-Z. Wu, C.-H. Tung, T. Zhang, *Adv. Mater.* **2019**, *31*, 1806482; e) J. Li, D. Wu, J. Iocozzia, H. Du, X. Liu, Y. Yuan, W. Zhou, Z. Li, Z. Xue, Z. Lin, *Angew. Chem., Int. Ed.* **2019**, *58*, 1985; f) J. Ran, J. Qu, H. Zhang, T. Wen, H. Wang, S. Chen, L. Song, X. Zhang, L. Jing, R. Zheng, S.-Z. Qiao, *Adv. Energy Mater.* **2019**, *9*, 1803402.
- [3] M.-Q. Yang, M. Gao, M. Hong, G. W. Ho, *Adv. Mater.* **2018**, *30*, 1802894.
- [4] a) Y. Wang, Y. Zhao, J. Liu, Z. Li, G. I. N. Waterhouse, R. Shi, X. Wen, T. Zhang, *Adv. Energy Mater.* **2020**, *10*, 1902860; b) G. Chen, R. Gao, Y. Zhao, Z. Li, G. I. N. Waterhouse, R. Shi, J. Zhao, M. Zhang, L. Shang, G. Sheng, X. Zhang, X. Wen, L.-Z. Wu, C.-H. Tung, T. Zhang, *Adv. Mater.* **2018**, *30*, 1704663.
- [5] a) L. Zhu, T. Ding, M. Gao, C. K. N. Peh, G. W. Ho, *Adv. Energy Mater.* **2019**, *9*, 1900250; b) M. Gao, C. K. Peh, H. T. Phan, L. Zhu, G. W. Ho, *Adv. Energy Mater.* **2018**, *8*, 1870114; c) P. Yang, K. Liu, Q. Chen, J. Li, J. Duan, G. Xue, Z. Xu, W. Xie, J. Zhou, *Energy Environ. Sci.* **2017**, *10*, 1923; d) M. Gao, L. Zhu, C. K. Peh, G. W. Ho, *Energy Environ. Sci.* **2019**, *12*, 841; e) X. Hu, J. Zhu, *Adv. Funct. Mater.* **2020**, *30*, 1907234; f) L. Zhou, Y. Tan, J. Wang, W. Xu, Y. Yuan, W. Cai, S. Zhu, J. Zhu, *Nat. Photonics* **2016**, *10*, 393; g) L. Zhou, X. Li, G. W. Ni, S. Zhu, J. Zhu, *Natl. Sci. Rev.* **2019**, *6*, 562; h) Y. Yang, X. Yang, L. Fu, M. Zou, A. Cao, Y. Du, Q. Yuan, C.-H. Yan, *ACS Energy Lett.* **2018**, *3*, 1165; i) Y. Lin, Z. Chen, L. Fang, M. Meng, Z. Liu, Y. Di, W. Cai, S. Huang, Z. Gan, *Nanotechnology* **2019**, *30*, 015402.

- [6] Y. Yang, X. Yang, L. Liang, Y. Gao, H. Cheng, X. Li, M. Zou, R. Ma, Q. Yuan, X. Duan, *Science* **2019**, *364*, 1057.
- [7] a) B. N. Nunes, O. F. Lopes, A. O. T. Patrocinio, D. W. Bahnemann, *Catalysts* **2020**, *10*, 126; b) S. Liang, L. Wen, S. Lin, J. Bi, P. Feng, X. Fu, L. Wu, *Angew. Chem., Int. Ed.* **2014**, *53*, 2951.
- [8] K. J. De France, T. Hoare, E. D. Cranston, *Chem. Mater.* **2017**, *29*, 4609.
- [9] X. Shan, A. Zhao, Y. Lin, Y. Hu, Y. Di, C. Liu, Z. Gan, *Adv. Sustainable Syst.* **2020**, *4*, 1900153.
- [10] a) Y. Xu, C. Zhang, L. Zhang, X. Zhang, H. Yao, J. Shi, *Energy Environ. Sci.* **2016**, *9*, 2410; b) M.-Q. Yang, L. Shen, Y. Lu, S. W. Chee, X. Lu, X. Chi, Z. Chen, Q.-H. Xu, U. Mirsaidov, G. W. Ho, *Angew. Chem., Int. Ed.* **2019**, *58*, 3077.
- [11] Y. Song, H. Wang, X. Gao, Y. Feng, S. Liang, J. Bi, S. Lin, X. Fu, L. Wu, *ACS Catal.* **2017**, *7*, 8664.
- [12] a) M.-Q. Yang, J. Wang, H. Wu, G. W. Ho, *Small* **2018**, *14*, 1703323; b) N. Zhang, X. Li, H. Ye, S. Chen, H. Ju, D. Liu, Y. Lin, W. Ye, C. Wang, Q. Xu, J. Zhu, L. Song, J. Jiang, Y. Xiong, *J. Am. Chem. Soc.* **2016**, *138*, 8928.
- [13] G. Sun, Z. Li, R. Liang, L.-T. Weng, L. Zhang, *Nat. Commun.* **2016**, *7*, 12095.
- [14] F. Zhao, X. Zhou, Y. Shi, X. Qian, M. Alexander, X. Zhao, S. Mendez, R. Yang, L. Qu, G. Yu, *Nat. Nanotechnol.* **2018**, *13*, 489.
- [15] a) J. Chen, H. Wang, Z. Zhang, L. Han, Y. Zhang, F. Gong, K. Xie, L. Xu, W. Song, S. Wu, *J. Mater. Chem. A* **2019**, *7*, 5493; b) X. Li, W. Li, Z. Zhuang, Y. Zhong, Q. Li, L. Wang, *J. Phys. Chem. C* **2012**, *116*, 16047.
- [16] a) L. T. Chiem, L. Huynh, J. Ralston, D. A. Beattie, *J. Colloid Interface Sci.* **2006**, *297*, 54; b) J. Shen, B. Yan, T. Li, Y. Long, N. Li, M. Ye, *Composites, Part A* **2012**, *43*, 1476.
- [17] a) P. Mu, Z. Zhang, W. Bai, J. He, H. Sun, Z. Zhu, W. Liang, A. Li, *Adv. Energy Mater.* **2019**, *9*, 1802158; b) E. Kolanthai, P. A. Sindu, D. K. Khajuria, S. C. Veerla, D. Kuppuswamy, L. H. Catalani, D. R. Mahapatra, *ACS Appl. Mater. Interfaces* **2018**, *10*, 12441.
- [18] X. Zhou, F. Zhao, Y. Guo, Y. Zhang, G. Yu, *Energy Environ. Sci.* **2018**, *11*, 1985.
- [19] a) X. Yang, Y. Yang, L. Fu, M. Zou, Z. Li, A. Cao, Q. Yuan, *Adv. Funct. Mater.* **2018**, *28*, 1704505; b) Y. Li, T. Gao, Z. Yang, C. Chen, W. Luo, J. Song, E. Hitz, C. Jia, Y. Zhou, B. Liu, B. Yang, L. Hu, *Adv. Mater.* **2017**, *29*, 1700981.
- [20] J. Wang, Y. Li, L. Deng, N. Wei, Y. Weng, S. Dong, D. Qi, J. Qiu, X. Chen, T. Wu, *Adv. Mater.* **2017**, *29*, 1603730.
- [21] M. Zhu, Y. Li, F. Chen, X. Zhu, J. Dai, Y. Li, Z. Yang, X. Yan, J. Song, Y. Wang, E. Hitz, W. Luo, M. Lu, B. Yang, L. Hu, *Adv. Energy Mater.* **2018**, *8*, 1701028.
- [22] Y. Liu, S. Yu, R. Feng, A. Bernard, Y. Liu, Y. Zhang, H. Duan, W. Shang, P. Tao, C. Song, T. Deng, *Adv. Mater.* **2015**, *27*, 2768.
- [23] L. Yan, Z. Gu, X. Zheng, C. Zhang, X. Li, L. Zhao, Y. Zhao, *ACS Catal.* **2017**, *7*, 7043.
- [24] a) R. Chen, F. Fan, T. Dittrich, C. Li, *Chem. Soc. Rev.* **2018**, *47*, 8238; b) M.-C. Wu, H.-C. Liao, Y.-C. Cho, G. Tóth, Y.-F. Chen, W.-F. Su, K. Kordás, *J. Mater. Chem. A* **2013**, *1*, 5715; c) W. Lu, K. Zeng, *Funct. Mater. Lett.* **2018**, *11*, 1830002; d) V. W. Bergmann, S. A. L. Weber, F. Javier Ramos, M. K. Nazeeruddin, M. Grätzel, D. Li, A. L. Domanski, I. Lieberwirth, S. Ahmad, R. Berger, *Nat. Commun.* **2014**, *5*, 5001.
- [25] M.-Q. Yang, N. Zhang, Y. Wang, Y.-J. Xu, *J. Catal.* **2017**, *346*, 21.
- [26] M. Gao, P. K. N. Connor, G. W. Ho, *Energy Environ. Sci.* **2016**, *9*, 3151.
- [27] Z. Gan, X. Wu, M. Meng, X. Zhu, L. Yang, P. K. Chu, *ACS Nano* **2014**, *8*, 9304.
- [28] Y. Shi, R. Li, Y. Jin, S. Zhuo, L. Shi, J. Chang, S. Hong, K.-C. Ng, P. Wang, *Joule* **2018**, *2*, 1171.
- [29] Y. Lin, H. Xu, X. Shan, Y. Di, A. Zhao, Y. Hu, Z. Gan, *J. Mater. Chem. A* **2019**, *7*, 19203.
- [30] G. Ni, G. Li, S. V. Boriskina, H. Li, W. Yang, T. Zhang, G. Chen, *Nat. Energy* **2016**, *1*, 16126.